

# Assessing the classicality of photon echo from excitons in lead halide perovskite nanocrystals

George Alkhalil,<sup>1</sup> Hendrik Rose,<sup>2</sup> Artur V. Trifonov,<sup>3,1</sup> Polina R. Sharapova,<sup>4</sup> Jan Sperling,<sup>2,4</sup> Dmitri R. Yakovlev,<sup>1</sup> Elena V. Kolobkova,<sup>5,6</sup> Maria S. Kuznetsova,<sup>3</sup> Marc Aßmann,<sup>1</sup> Manfred Bayer,<sup>1,7</sup> Torsten Meier,<sup>2,4</sup> and Ilya A. Akimov<sup>1</sup>

<sup>1</sup>*Experimentelle Physik 2, Technische Universität Dortmund, 44227 Dortmund, Germany*

<sup>2</sup>*Institute for Photonic Quantum Systems (PhoQS), Paderborn University, D-33098 Paderborn, Germany*

<sup>3</sup>*Spin Optics Laboratory, St. Petersburg State University, 198504 St. Petersburg, Russia*

<sup>4</sup>*Department of Physics and Center for Optoelectronics and Photonics Paderborn (CeOPP), Paderborn University, D-33098 Paderborn, Germany*

<sup>5</sup>*ITMO University, 199034 St. Petersburg, Russia*

<sup>6</sup>*St. Petersburg State Institute of Technology, 190013 St. Petersburg, Russia*

<sup>7</sup>*Research Center FEMS, Technische Universität Dortmund, 44227 Dortmund, Germany*

Photon echo (PE) spectroscopy is a powerful technique for probing decoherence mechanisms and charge carrier dynamics in semiconductor systems. Beyond traditional coherence measurements, characterizing the photon statistics of the echo signal is important for assessing its potential in quantum information applications and understanding the underlying quantum mechanical processes. Here, we study the photon statistics of PE signals generated by excitons in ensembles of lead halide perovskite CsPbI<sub>3</sub> nanocrystals at cryogenic temperature of 2 K using continuous-variable quantum state optical tomography based on homodyne detection. Pronounced Rabi oscillations of PE amplitude allow us to evaluate the statistics for various pulse areas in the excitation sequence. The damping of the oscillations with increasing pulse area is attributed to spatial excitation inhomogeneity and excitation-induced dephasing. Despite the large ensemble of optically addressed excitons, the efficiency of generated PE signals is low which is attributed to complex energy structure of excitons and non-radiative recombination channels in CsPbI<sub>3</sub> nanocrystals. We analyze the statistical characteristics of PE via the second-order correlation function  $g^{(2)}(0)$  and the characteristic function for different combinations of the areas of the excitation pulses. Our results show that  $g^{(2)}(0) = 1$ , and the characteristic function of the PE signal corresponds to classical behavior. Despite the relatively low efficiency, the photon echo exhibits a high degree of coherence and minimal classical noise, consistent with Poissonian statistics.

## I. INTRODUCTION

Metal halide perovskite nanocrystals (NCs) have recently emerged as a promising class of materials for optoelectronic and quantum optical devices [1]. The elementary optical excitations in lead halide perovskites are excitons, which determine their exceptional properties, including high photoluminescence quantum yields, tunable emission wavelengths, and strong light–matter interactions [1–7]. Recent studies have demonstrated their potential for single-photon generation and strong nonlinear optical responses, making them a robust platform for exploring fundamental light–matter interactions and for possible applications in quantum optical devices [8–12].

Photon echo is considered as a powerful technique for probing coherent dynamics of excitons in perovskite semiconductors [13–17]. It relies on resonant excitation of excitons by a sequence of short optical pulses, where the rephasing process restores the coherent polarization induced by the first pulse, resulting in the emission of a delayed echo pulse [18–21]. The photon echo technique allows the measurement of coherence times and evaluation of the homogeneous linewidth of exciton in ensembles of NCs, despite strong inhomogeneous broadening. In the context of perovskite nanocrystals, photon echo exper-

iments revealed comprehensive quantum dynamics such as quantum beats originating from exciton fine structure splitting [14, 17]. However, beyond measuring the photon echo amplitude, analyzing and characterizing the photon statistics of the echo signal is of particular importance for assessing its suitability in quantum optical applications. In particular, for applications such as quantum memories, it is essential that the storage and retrieval process does not introduce additional noise or alter the nonclassical photon statistics of the input field. Furthermore, statistical properties of the photon echo can provide a deeper understanding of the underlying quantum mechanical processes governing coherence and dephasing in the studied materials.

In the context of quantum optics, photon echoes deserve special attention as a manifestation of coherent light–matter interaction and collective emission phenomena. While photon echoes have been extensively discussed in the framework of quantum memory protocols in rare-earth-doped crystals and atomic systems [22–24], they also provide a unique platform for exploring quantum optical effects at the level of weak and even single-photon fields [25]. It has been shown that the conventional two-pulse photon echo is unsuitable for quantum memory applications due to strong quantum noise origi-

nating from spontaneous emission [26, 27]. Nevertheless, the underlying processes give rise to a variety of intrinsically quantum-optical phenomena, e.g., rephased amplified spontaneous emission [28], which can exhibit nontrivial temporal correlations and expected to strongly influence the photon statistics of the emitted field. However, despite these developments, quantum tomography of the emitted fields in photon-echo protocols has received little attention as most studies have focused on single-photon excitation and photon-counting detection schemes.

In semiconductor systems, photon echo has been demonstrated up to the level of single quantum emitters, including self-assembled quantum dots [29–33]. These measurements were focused on the acquisition of phase-resolved classical fields using heterodyne detection and two-dimensional Fourier spectroscopy. A key advantage of semiconductor quantum emitters is the large oscillator strength of excitons, leading to short radiative lifetimes below 1 ns and enabling experiments at very high repetition rates, reaching up to 1 GHz [34]. This makes semiconductor platforms particularly attractive for systematic investigations of photon-echo statistics using continuous-variable quantum state tomography [35–38]. In this context, homodyne detection represents an excellent tool for evaluating the statistical and correlation properties of photon-echo fields, offering high temporal resolution together with fast operation enabled by high repetition rates.

In this work, we modify our previously developed real-time optical homodyne detection scheme [38] and employ it to investigate the photon statistics of photon echo signals generated in ensembles of quantum emitters based on perovskite  $\text{CsPbI}_3$  nanocrystals. The paper is organized as follows. Section II introduces the investigated sample (II A) and two-pulse photon echo experimental setup (II B). The details on homodyne detection and evaluation of phase-resolved quadratures are described in Sec. II C. The main experimental results in Sec. III are divided in two parts. First, in Sec. III A, we demonstrate Rabi oscillations in the PE signal, a result that has not yet been reported for perovskite NCs. The damping of the Rabi oscillations is partly caused by spatial inhomogeneity of the excitation (transverse beam profile and the finite optical thickness of the sample) as well as by excitation-induced dephasing, as evidenced by the dependence of optical coherence time  $T_2$  on the excitation strength. Second, in Sec. III B, we evaluate the correlation and characteristic functions of the PE signal for excitation pulses of different areas by analyzing a set of phase-sensitive quadratures acquired via homodyne detection. Sec. III C presents the theoretical modeling by a quantized free-space multimode description. The discussion in Sec. III D highlights the main results, namely the classical behavior of two-pulse photon echoes under excitation with laser pulses and negligible contribution of spontaneous emission due to use of homodyne detection with pulse duration much shorter than the exciton lifetime. Here, we also address the origin of low effi-

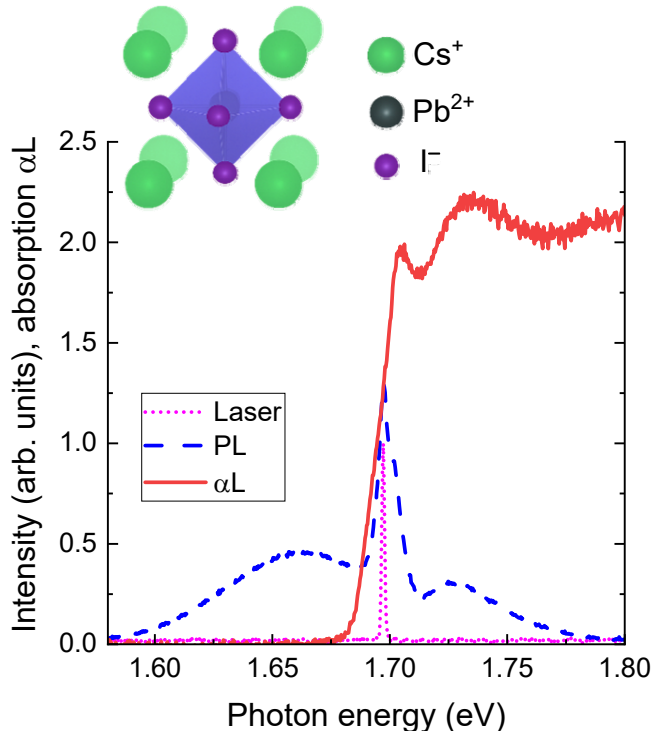


FIG. 1. Photoluminescence (PL, dashed blue line) and absorption coefficient  $\alpha(h\nu)L$  (solid red line) spectra of a  $\text{CsPbI}_3$  nanocrystals measured at  $T = 2$  K. The PL spectrum was measured in back reflection geometry under excitation with photon energy of 2.33 eV. The laser spectrum used in the PE measurements is shown with dotted magenta line. Inset shows  $\text{CsPbI}_3$  perovskite crystal structure.

ciency of photon echo in  $\text{CsPbI}_3$  NCs. A conclusion and outlooks are given in Sec. IV.

## II. SAMPLE AND EXPERIMENTAL SETUP

### A. Sample

The investigated sample contains  $\text{CsPbI}_3$  nanocrystals embedded in fluorophosphate  $\text{Ba}(\text{PO}_3)_2\text{-AlF}_3$  glass. The sample (reference number EK8) was synthesized by rapid cooling of a glass melt enriched with the components needed for the perovskite crystallization. More details on the preparation method of the sample are given in Refs. 39 and 40. The average diameter of the nanocrystals is about 10 to 15 nm. The sample thickness  $L$  is about 200  $\mu\text{m}$ . The absorption and photoluminescence (PL) spectra of the sample measured at the temperature of  $T = 2$  K are shown in Fig. 1. The absorption band is characterized by an edge located at a photon energy of about  $h\nu = 1.70$  eV. The PL comprises a sharp peak approximately at the same energy 1.697 eV, which is superimposed on a broader peak in the spectral range

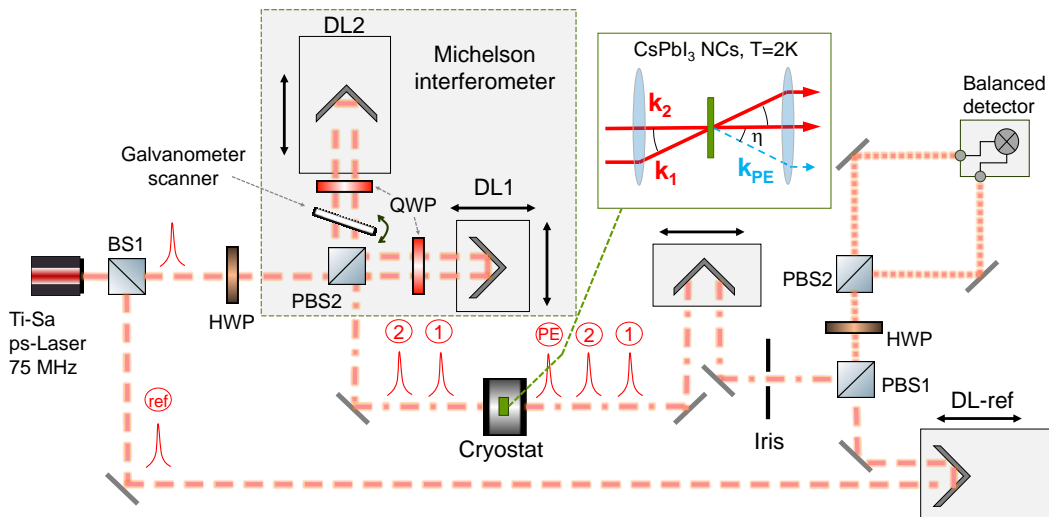


FIG. 2. Schematic presentation of the experimental setup for measuring and characterizing the photon echo. Notations: BS – beam-splitter; PBS – polarizing beamsplitter; DL – delay line, HWP – half waveplate, QWP – quarter waveplate. PE – photon echo, ref – reference. The inset shows a close-up of the sample in the cryostat with the excitation and four-wave mixing beam geometry.

of 1.6–1.8 eV. Such inhomogeneous spectral broadening arises from variations in the size of the nanocrystals. Moreover, the presence of narrow and broad PL bands is attributed to two sub-ensembles of NCs with different sizes. The narrow absorption peak originates, possibly from one of the sub-ensembles of NCs with a narrower size distribution. Subsequently, the laser used in PE experiments was tuned to the energy 1.697 eV for performing the experiment (see Fig. 1).

## B. Photon Echo Setup

The experimental setup is illustrated in Fig. 2. The setup includes a Ti:sapphire laser (Mira-900), which is tunable in the range of 700–990 nm and pumped by a 532 nm continuous-wave laser. The laser generates picosecond pulses with a duration of about 3 ps at a repetition frequency of 75 MHz and is tuned to a photon energy of 1.697 eV. We intentionally use spectrally narrow optical pulses with a full width at half maximum of about 0.6 meV in order to address signals related to the zero-phonon exciton line with long-lived coherence on the order of hundreds of picoseconds. This allows us to establish Rabi flopping of excitons in nanocrystals, which is otherwise difficult when using femtosecond optical pulses, where multiple exciton-polaron states have to be considered [17].

The laser beam is split by beam splitters into two excitation pulses using a Michelson interferometer (labeled as 1 and 2 in Fig. 2) and one reference pulse (labeled as ref in Fig. 2). The delay time between optical pulses is controlled using mechanical translation stages ( $DL_1$ ,

$DL_2$ ,  $DL_{\text{ref}}$ ). Specifically, the second pulse is delayed by an interval  $\tau_{12}$  relative to the first pulse, and the reference pulse is delayed by  $\tau_{\text{ref}}$  relative to the first pulse. We can switch between the co-linear and non-colinear geometry by transversely shifting the retroreflector on  $DL_1$ , i.e. by changing the distance between beams exiting the interferometer. In this work, the non-colinear geometry was used to minimize stray light from the excitation pulses. The first pulse is transversely shifted by 3 mm relative to the second pulse. This shift results in a difference in their incidence angles of  $\eta = 0.03$  rad at the sample, after passing through the focusing lens placed before the cryostat with the sample (see the inset of Fig. 2). Note that the second beam arrives under normal incidence, and, therefore,  $\eta$  is defined by the angle of incidence of the first pulse. The PE signal was measured in the transmission geometry and collected in the phase-matching direction defined by  $\mathbf{k}_{\text{PE}} = 2\mathbf{k}_2 - \mathbf{k}_1$ . In this case, when perfect phase matching (co-linear geometry), corresponding to  $\Delta k = 0$ , is not satisfied, the resulting decrease in the efficiency of the PE generation can be estimated using  $I/I_0 = \text{sinc}^2(\frac{\Delta k L}{2}) = 0.62$ , where  $\Delta k L = 2\pi n L \eta^2 / \lambda = 2.34$ , is the phase mismatch ( $\lambda$  is the excitation wavelength, and  $n = 1.5$  is the refractive index of the fluorophosphate glass) [41].

Measurements were performed in the polarization configuration, where the first and second pulses are linearly cross-polarized, while the detection polarization is parallel to the polarization of the first pulse. This scheme allows for further suppression of the stray light from the second pulse by filtering the signal using a polarizer in the detection path. In this configuration, however, the PE signal originating from excitons is typically weaker.

For exciton transitions, signals are generally observed only in the co-polarized configurations, consistent with the expectation for a V-type energy scheme [42]. In the cross-polarized configuration, the exciton contribution becomes observable due to exciton fine-structure splitting, random orientation of nanocrystals in the ensemble, and dephasing arising from fluctuations of the fine-structure splitting among NCs of different sizes [14, 43]. As recently demonstrated for similar CsPbI<sub>3</sub> nanocrystals [17], these effects allow one to observe the PE signal even in cross-polarized configuration, albeit with an electric field amplitude about five times smaller than in the co-polarized case.

The sample was placed in a helium bath cryostat and kept at a temperature  $T = 2$  K. The excitation pulses are focused onto the sample within a spot diameter of approximately  $50 \mu\text{m}$  using a convex spherical achromatic doublet lens with a focal length of 100 mm. From these parameters, we can estimate the number of NCs addressed in the experiment. The NC density in the sample is approximately  $10^{15} \text{cm}^{-3}$  [40]. The illuminated volume amounts to  $V = 4 \times 10^{-7} \text{cm}^3$ . However, due to the strong inhomogeneous broadening, only a small fraction of NCs is resonant with the excitation pulse. This fraction can be estimated from the ratio of the laser spectral width  $\approx 0.6$  meV (full width at half maximum, FWHM) to the PL linewidth (FWHM  $\approx 50$  meV) which is about  $10^{-2}$ . Thus, we estimate a number of resonantly addressed NCs in the order of  $N_x \approx 5 \times 10^6$ .

The phase of the second pulse is modulated using a single-axis scanning galvanometer that rotates a glass plate placed in one arm of the Michelson interferometer at an incidence angle of approximately  $20^\circ$ . The glass plate undergoes angular modulation following a sawtooth waveform, with an amplitude of approximately  $0.5^\circ$  at a frequency of 100 Hz (see Fig. 3(a)). Each half-period of the oscillation changes the phase by about  $11\pi$ , resulting in a linear phase sweep and a modulation of the cross-correlation between the second laser beam and the reference at approximately 1.1 kHz. Note that the phase change is nonlinear due to the acceleration and deceleration between the deflection points in the glass plate movement. Therefore, the acquisition window was set to span a phase interval of  $2\pi$  within the central region of the glass-plate motion. In this defined region, the phase change can be considered linear, which simplifies the processing of the acquired data.

Phase modulation serves two key purposes in our experiment. First, modulating the phase of the second pulse also modulates the phase of the PE, and this enables us to perform a phase sensitive measurement of the PE quadrature, which will be described in detail below in Sec. II C. Second, it allows us to distinguish between different contributions of optical fields in the detection channel. In particular, contributions from the coherent PE signal, coherent stray light and incoherent signals such as spontaneous emission can be evaluated separately using the phase modulation (phase cycling) approach.

Coherent contributions can be distinguished according to the frequency phase-matching condition, the phase of the photon echo is given by a combination of the phases of the excitation pulses  $\varphi_{\text{PE}} = 2\varphi_2 - \varphi_1$ . As a result, modulating the phase of the second pulse at frequency  $f$  leads to different modulation frequencies of the various signals: the PE signal and coherent stray light contributions are modulated at frequencies  $f_{\text{PE}} = 2f$  and  $f$ , respectively, while there is no modulation of the signal arising due to spontaneous emission. In some measurements, where only the amplitude of the PE signal is measured, we employ filtering at  $2f$ , and acquire the PE signal amplitude through a lock-in detection algorithm.

In the detection section of the setup, the PE signal is combined with a strong reference beam at a polarizing beam splitter (PBS1 in Fig. 2), and the polarization of both signals is rotated by  $45^\circ$ . The intensity of the reference beam is 1.5 mW, where, at this power level, the shot noise of the reference field dominates over the electronic noise from the detector and electronics. The mixed signal is then split equally into two channels before reaching a balanced photodetector. This configuration allows us to measure the cross-correlation between the reference pulse and the PE signal.

### C. Homodyne Detection

We use the homodyne detection scheme described in Refs. 37. A weak input signal is mixed with a strong local oscillator (in this work the reference is used as local oscillator). These signals are typically combined using a beam splitter, which induces a  $\pi$  phase shift between the signals at the output. After the beam splitter, the combined signal is detected by photodetectors. The balanced photodetection provides the difference in the intensities  $n_-$  measured at its different channels. The signal  $n_-$  is directly proportional to the quadrature of the weak signal,  $q_\varphi$ , with the proportionality factor determined by the amplitude of local oscillator,  $\alpha_{\text{LO}}$ :

$$\hat{q}_\varphi = \frac{\hat{n}_-}{\sqrt{2}\alpha_{\text{LO}}} \quad (1)$$

where  $\alpha_{\text{LO}}$  is the amplitude of the local oscillator.

These quadratures can then be used to calculate various characteristics of the light field, including photon statistics and the second-order correlation function  $g^{(2)}(0)$ . The second-order correlation function is a measure of the statistical properties of a light field. For a coherent state, we have  $g^{(2)}(0) = 1$ , while for non-classical light, such as a single-photon emitter, we find  $g^{(2)}(0) < 1$ , and, in the case of a thermal state, we obtain  $g^{(2)}(0) > 1$ . In our experiment, we calculate  $g^{(2)}(0)$  using the following quadrature-based formula [36]:

$$g^{(2)}(\tau = 0, t) = \frac{\langle \hat{a}_s^\dagger \hat{a}_s^\dagger \hat{a}_s \hat{a}_s \rangle}{\langle \hat{a}_s^\dagger \hat{a}_s \rangle^2} = \frac{4\langle \hat{q}_\varphi^4 \rangle - 12\langle \hat{q}_\varphi^2 \rangle + 3}{6(\langle \hat{q}_\varphi^2 \rangle - \frac{1}{2})^2}. \quad (2)$$

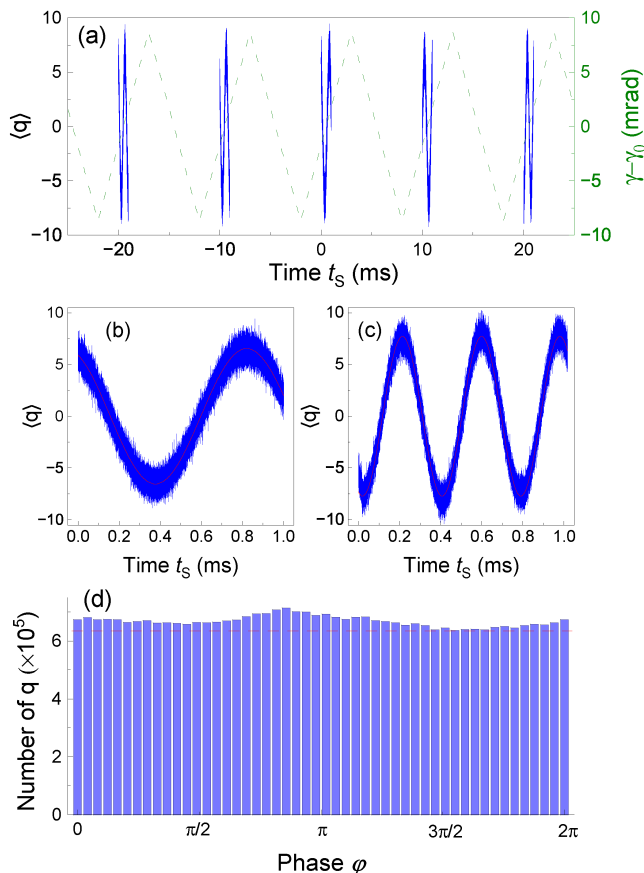


FIG. 3. (a) The blue curve represents a cross-correlation measurement between the reference and attenuated second excitation pulse (about 20 photons per pulse). The green curve is the corresponding deviation angle of the oscillating glass plate around the incidence angle  $\gamma_0 = 0.27$  rad. Each segment (b) represents about  $7 \times 10^4$  quadrature points collected at the center of the glass plate's linear ramp. The blue curve shows the experimental data and the red curve is the sinusoidal fitting curve used to determine the phase for each quadrature point. (c) The segment shape for the PE signal, illustrating the double-frequency modulation compared to single frequency modulation for the excitation laser pulse shown in (b). (d) A histogram shows the initial unequal distribution of the number of quadrature, and the red dashed line illustrates the level of the distribution of quadrature samples after truncation.

The averaging of quadratures occurs over a large array of accumulated experimental values [57]. This expression is valid only for phase-averaged measurements, which allows for the assumption that  $\langle q_\varphi \rangle = 0$ . The condition is naturally satisfied when the signal and the local oscillator originate from independent sources, resulting in a random relative phase. However, the photon echo signal retains a well-defined phase relationship to the local oscillator, as both are derived from the same laser source. To meet the phase-averaging requirement in our case, the following data processing method was implemented.

Figure 3 illustrates the data acquisition and process-

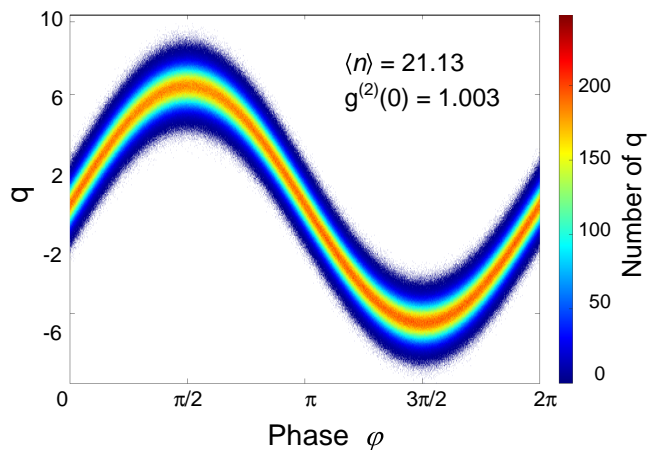


FIG. 4. The histogram of phase-resolved quadratures for a highly attenuated second excitation laser pulse. The figure is based on  $3 \times 10^7$  acquired data points.

ing method, showing a cross-correlation measurement between the reference and a strongly attenuated second excitation pulse (about 20 photons per pulse) serving as the signal. The data acquisition is conducted in discrete segments, with each segment corresponding to about  $7 \times 10^4$  quadrature points collected at the center of the glass plate's linear ramp. Figure 3(a) (blue curve) shows five segments of an acquired data sample and the corresponding deviation angle of the oscillating glass plate (green curve) in real time. For each segment, a sinusoidal function of the form  $A \sin(2\pi f t_s + \delta)$  is fitted to the data to extract the phase information, where  $t_s$  is the time stamp (see red curve in Fig. 3(b)). In the case of PE, the fitting function has the form  $A \sin(4\pi f t_s + \delta)$  (see Fig. 3(c)). Each measured quadrature value is then assigned to a corresponding phase  $\varphi$  between 0 and  $2\pi$ . Due to the phase fluctuations of the reference, different data segments cover different phase ranges. Therefore, as shown in Fig. 3(d), different phase regions accumulate different numbers of quadratures. To achieve uniform phase sampling, we randomly truncate the number of quadrature points in the overrepresented regions, ensuring a homogeneous distribution of quadrature measurements across all phases (Fig. 3(d) red dashed red line).

By using an equal number of quadratures across all phases, the condition for phase-averaged measurements  $\langle q_\varphi \rangle = 0$  is effectively satisfied, allowing us to apply Eq. (2). After this step, the distribution of quadrature values as a function of phase can be plotted. Figure 4 shows an example of acquired quadratures for the attenuated second excitation laser pulse. By applying Eq. (2) on the quadrature set in Fig. 4, we obtain a value of  $g^{(2)}(0) = 1.003 \pm 0.0001$  for the laser pulse which agrees with Poisson statistics expected for classical laser source. For phase randomized quadratures, we also calculate the average photon number per pulse  $\langle n \rangle = \langle q^2 \rangle - 0.5 = 21.13$ , where we used the expectation

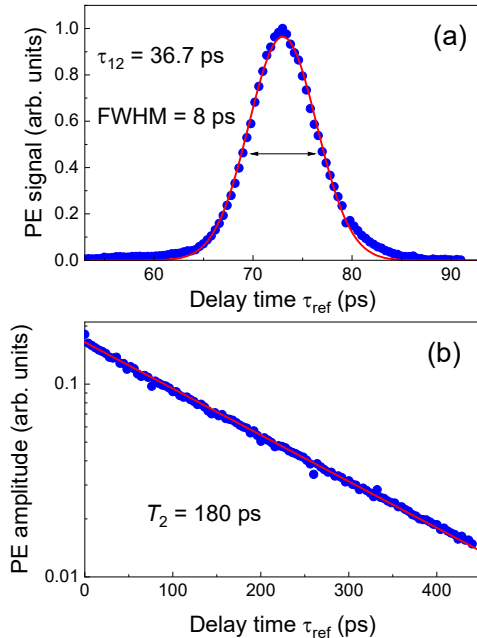


FIG. 5. The PE temporal profile (a) and PE amplitude decay (b) measured for  $h\nu = 1.697$  eV,  $T = 2$  K,  $\tau_{12} = 36.7$  ps,  $A_1 = 4.5$  pJ<sup>1/2</sup>,  $A_2 = 9.0$  pJ<sup>1/2</sup>. Dots correspond to experimental data and lines to the fit with Gaussian (a) and exponential (b) functions.

value of all squared quadratures. This value is in agreement with  $\alpha_S^2/2$  obtained from sinusoidal fit with with amplitude  $\alpha_S = 6.50$  in Fig. 4.

### III. RESULTS AND DISCUSSION

#### A. Rabi Oscillations of the Photon Echo

Scanning the time delay between the first pulse and the reference pulse  $\tau_{\text{ref}}$ , while keeping delay time  $\tau_{12}$  constant constitutes a measurement of the temporal profile of the PE pulse. Figure 5(a) shows the temporal profile of the PE pulse at a delay time of  $\tau_{12} = 36.7$  ps. The symbols represent experimental data, while the red curve is a Gaussian fit with a full width at half maximum (FWHM) of  $\sigma_{\text{PE}} \approx 8$  ps. The measured signal represents the cross-correlation between the optical fields of the PE and reference pulses, i.e. the convolution of these pulses. The width of the PE profile therefore reflects the spectral broadening of the excited ensemble, which is determined by the spectral width of the laser. Assuming Gaussian pulse shapes, we estimate the FWHM duration of the PE intensity pulse as  $\sqrt{\sigma_{\text{PE}}^2/2 - \tau_d^2} = 4.8$  ps, where  $\tau_d = 3$  ps is the laser pulse duration. This is consistent with the

regime where the inhomogeneous broadening of the ensemble is substantially broader than the laser pulse spectrum.

A simultaneous scan of  $\tau_{12}$  and  $\tau_{\text{ref}} = 2\tau_{12}$  allows one to measure the decay of the PE amplitude and evaluate the exciton coherence time  $T_2$ . These data are shown in Fig. 5(b). Fitting the experimental curve in Fig. 5(b) with an exponential function  $\propto \exp(-2\tau_{12}/T_2)$  (red curve) yields  $T_2 = 180$  ps. The value is in agreement with the coherence times measured in the range from 150 to 330 ps in similar CsPbI<sub>3</sub> NCs [17]. For higher excitation levels, the decay of the PE amplitude becomes shorter and non-monotonic indicating the importance of excitation induced dephasing, discussed at the end of this section (see also Appendix A).

In order to measure Rabi oscillations, PE transients similar to the one shown in Fig. 5(a) are recorded as a function of the pulse area of one of the two excitation pulses,  $\Theta_i$  ( $i = 1, 2$ ), while the area of the other pulse is kept constant. The pulse area is defined as  $\Theta = \int_{-\infty}^{+\infty} \Omega_R(t) dt$ , where  $\Omega_R(t) = d_{12}E(t)/\hbar$  is the Rabi frequency with  $E(t)$  being the time-dependent electric field amplitude of an optical pulse, and  $d_{12}$  is the dipole matrix element of the optical transition. The area of the pulses is proportional to the pulse amplitudes  $A_i$ , which we define as the square root of the pulse energy. The variation of amplitudes  $A_i$  is accomplished by attenuation of their intensities using half-wave and quarter-wave plates in combination with PBS as part of the Michelson interferometer in Fig. 2. By scanning the areas of the incident pulses and measuring the temporal profiles of the photon echo, we observe Rabi oscillations displayed as two-dimensional images in Fig. 6.

When the first pulse amplitude  $A_1$  is varied at  $A_2 = 9.0$  pJ<sup>1/2</sup>, the PE transients reveal a complex two-dimensional picture with a split PE profile similar to that observed recently in a CdTe/(Cd,Mg)Te single quantum well and (In,Ga)As quantum dots [44, 45]. The first maximum of the Rabi oscillations for  $A_1 = 4.5$  pJ<sup>1/2</sup> corresponding to  $\Theta_1 \approx \pi/2$  is centered at  $2\tau_{12} \approx 73.4$  ps and is well described by a single pulse of Gaussian shape. However, the second maximum at  $A_1 = 11.5$  pJ<sup>1/2</sup> is advanced by 5.2 ps. The third maximum of Rabi oscillations at  $A_1 > 16$  pJ<sup>1/2</sup> appears to be also shifted by 3 ps (see Fig. 6(a)). This behavior is well established in the case of photon echoes with strong inhomogeneous broadening of optical transitions that is larger than the spectral width of the laser. In this case, there is a considerable dephasing during the action of the laser pulse which depends on its area. As a result, the temporal profile of echo experiences significant variations in time as studied in detail in Refs. 45–47.

When the amplitude of the second pulse  $A_2$  is varied at  $A_1 = 4.5$  pJ<sup>1/2</sup>, the PE maximum has no detectable shift, as can be seen in Fig. 6(b), being in agreement with previous studies in InGaAs quantum dots [46–48]. Here, however, only the first maximum of Rabi oscillations at  $A_2 = 9.0$  pJ<sup>1/2</sup> ( $\Theta_2 \approx \pi$ ) is pronounced, while the sec-

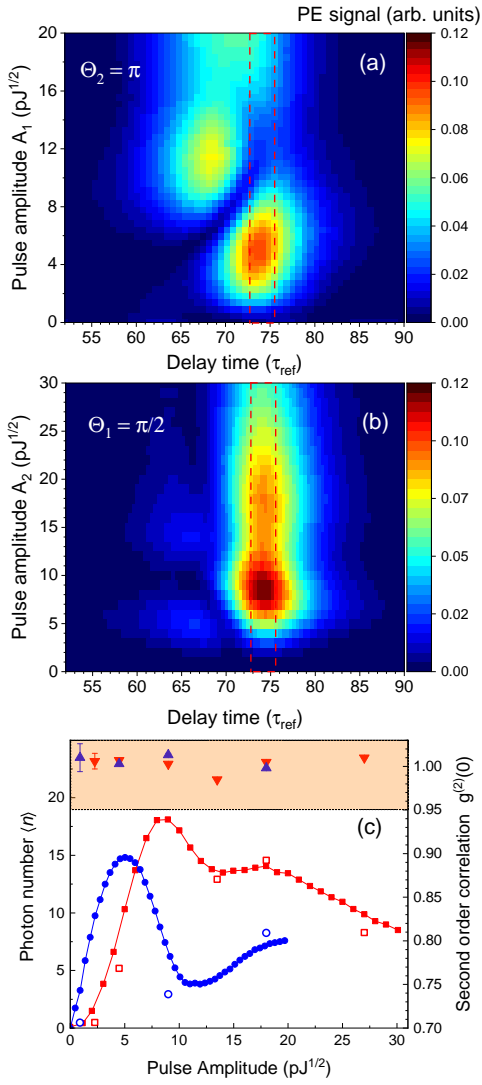


FIG. 6. (a) Rabi oscillations of PE amplitude. Measurements of PE transients (a) as a function of pulse amplitude  $A_1$  at  $A_2 = 9 \text{ pJ}^{1/2}$  corresponding to pulse area  $\Theta_2 \approx \pi$  and (b) as a function of pulse amplitude  $A_2$  at  $A_1 = 4.5 \text{ pJ}^{1/2}$  corresponding to pulse area  $\Theta_1 \approx \pi/2$ . (c) PE signal at  $\tau_{\text{ref}} = 2\tau_{12} = 73.4 \text{ ps}$  as a function of pulse amplitudes  $A_1$  and  $A_2$ . The data are evaluated within the time window of 3 ps centered at  $2\tau_{12}$ , as indicated by red rectangles in panels (a) and (b). Circles and squares correspond to variation of  $A_1$  and  $A_2$ , respectively. Open symbols correspond to the number of photons evaluated in the homodyne measurement ( $\tau_{\text{ref}} = 2\tau_{12} = 73.4 \text{ ps}$ ). Triangles correspond to the right axis and show the results of second-order correlation measurements summarized in Table I.

and one around  $A_2 = 18 \text{ pJ}^{1/2}$  ( $\Theta_2 \approx 2\pi$ ) is very weak. This is more easily visible in Fig. 6(c), where the cross sections of the two-dimensional plots of Rabi oscillations as a function of both pulse amplitudes are plotted.

We observe that an increase in the area of either excitation pulse leads to a damping of the photon echo signal. One of the reasons for such damping is the spatial in-

TABLE I.  $g^{(2)}(0)$  and average photon number  $\langle n \rangle$  measured for different pulse areas  $\Theta_1$  and  $\Theta_2$ .  $\tau_{\text{ref}} = 2\tau_{12} = 73.4 \text{ ps}$ .

$\Theta_1$	$\Theta_2$	$g^{(2)}(0)$	$\langle n \rangle$
$\frac{\pi}{10}$	$\pi$	1.010	0.47
$\frac{\pi}{2}$	$\frac{\pi}{4}$	1.006	0.48
	$\frac{\pi}{2}$	1.007	5.17
	$\pi$	1.003	30.3
	$\frac{3\pi}{2}$	0.985	12.9
$\pi$	$2\pi$	1.005	14.5
	$3\pi$	1.010	8.29
$\pi$	$\pi$	1.013	2.93
$2\pi$	$\pi$	0.998	8.26

homogeneity of the excitation, which includes both the Gaussian beam profile in the plane of the sample [44] and notable absorption along the propagation direction due to the finite optical thickness of the sample (see Fig. 1) [26]. In addition, excitation-induced dephasing plays an important role in our data, as manifested by the power dependence of the photon echo decay curves, where  $T_2$  decreases non-monotonically from 210 to 100 ps, as discussed in Appendix A.

## B. Second-Order Correlation and Characteristic Function

Here, we evaluate the results of quadrature measurements of the detected signals for different delay times  $\tau_{12}$ ,  $\tau_{\text{ref}}$ , and pulse areas  $A_1$ ,  $A_2$ . The quadratures are obtained using the procedure described in Section II C. First, we calculate the correlation function  $g^{(2)}(0)$  and photon number at the delay time corresponding to the PE maximum ( $\tau_{\text{ref}} = 2\tau_{12} = 73.4 \text{ ps}$ ), which are summarized in Table I. The average number of detected photons per PE pulse is also shown in Fig. 6(c) with open symbols. We notice in Table I that while the photon number changes in accordance with previously described Rabi flops when changing  $\Theta_1$  or  $\Theta_2$ , the  $g^{(2)}(0)$  is always  $\approx 1$ . This indicates that the photon echo signal from the perovskite nanocrystals sample exhibits classical photon statistics, which is consistent with the fact that the PE is coherent emission from the ensemble of emitters under excitation with a sequence of laser pulses. In addition, we measured the quadratures at the expected PE maximum when the first pulse is blocked. This results in  $\langle q \rangle = 0$  and  $\langle q^2 \rangle = 0.5$ , which corresponds to vacuum fluctuations. This value was obtained for all  $\Theta_2$  presented in Table I. The results also coincide with the data measured at  $\tau_{\text{ref}} < 2\tau_{12}$ , i.e., away from the PE pulse for all the different combinations of  $\Theta_1$  and  $\Theta_2$  presented in Table I.

Next, we calculate the characteristic function of the PE signal. The characteristic function is proved to be an

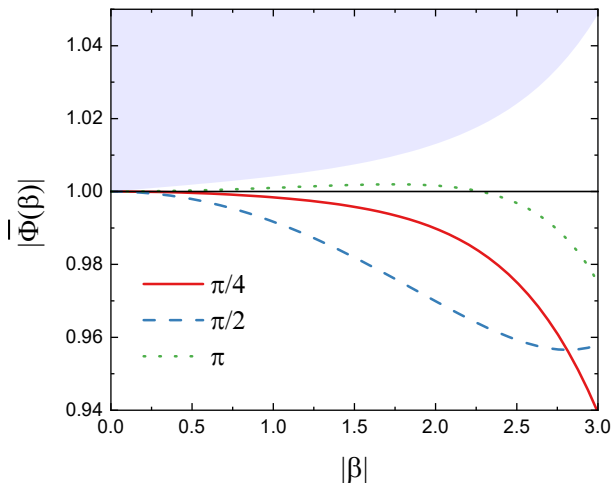


FIG. 7. Characteristic function  $|\bar{\Phi}(\beta)|$  for photon echo signal obtained using Eq. (3). Pulse areas correspond to  $\Theta_1 = \pi/10$  and  $\Theta_2 = \pi$ . The results are shown for different phases  $\varphi = \pi/4, \pi/2$ , and  $\pi$ . The shaded area corresponds non-classical region where a one standard deviation is added to the boundary  $|\Phi(\beta)| = 1$  according to Eq. (5).

effective criterion for detecting the deviation from classicality, particularly in cases where other conventional criteria fail [49, 50]. It is defined as the Fourier transform of the Glauber-Sudarshan P-function, which provides a quasi-probability distribution in phase space. The characteristic function  $\Phi(\beta)$  can be estimated from quadrature measurements using [49]

$$\bar{\Phi}(\beta) = \frac{1}{N} e^{\frac{|\beta|^2}{4}} \sum_{j=1}^N e^{i|\beta|q_j}, \quad (3)$$

where  $q_j$  are the quadratures measured at some specific phase  $\varphi$ ,  $N$  is the total number of quadratures for given  $\varphi$ . The variance of the expectation value of the characteristic function is defined as

$$\sigma^2(\bar{\Phi}(\beta)) = \frac{1}{N} \left[ e^{\frac{|\beta|^2}{2}} - |\bar{\Phi}(\beta)|^2 \right]. \quad (4)$$

The nonclassical boundary is usually defined as the range of one standard deviation added to the characteristic function of the vacuum,  $|\Phi_{\text{vac}}(\beta)| = 1$  [51, 52]:

$$|\bar{\Phi}(\beta)| > 1 + S \sigma(\bar{\Phi}(\beta)). \quad (5)$$

This means that for a nonclassical state, this inequality should be satisfied at least at one point  $\beta$  and with a minimum significance of  $S = 1$ . Conversely,  $|\Phi(\beta)| \leq 1$  holds true withing error margins for classical light. Note that higher-order criteria in terms of the characteristic function form a hierarchy of necessary and sufficient criteria for observing nonclassicality [51, 52].

In our analysis, Eq. (3) is applied to quadratures within a phase window of  $0.04\pi$  centered at  $\varphi = \pi/4, \pi/2$ , and  $\pi$ .

This subset included approximately  $3 \times 10^4$  quadrature points. The characteristic function of the photon echo is found to be within the classical region as shown in Fig. 7. Similar results were obtained for all  $\Theta_1$  and  $\Theta_2$  indicated in Table I. This further supports the observations from the  $g^{(2)}(0)$  measurements. The data indicate that, under the present experimental conditions, the photon echo exhibits purely classical features, while still preserving the coherence of the optical excitation.

### C. Theoretical Modeling

We model the sample as a thin sheet of inhomogeneously broadened two-level systems (TLS) located at  $z = 0$ , coupled to a multimode quantum light state. The matter is described by the coherence operator  $\hat{\sigma}_-(\Delta, t)$  for emitters with detuning  $\Delta$ , and the field by the photon annihilation operator  $\hat{a}(\omega, t)$  for mode frequency  $\omega$ . The inhomogeneous distribution of the TLS is denoted by  $f(\Delta)$  and the light-matter coupling by  $g$ .

In the weak-excitation regime, the mean values follow [53]

$$\frac{\partial}{\partial t} \langle \hat{\sigma}_-(\Delta, t) \rangle = -i\Delta \langle \hat{\sigma}_-(\Delta, t) \rangle + i s \int d\omega g \langle \hat{a}(\omega, t) \rangle, \quad (6)$$

$$\frac{\partial}{\partial t} \langle \hat{a}(\omega, t) \rangle = -i\omega \langle \hat{a}(\omega, t) \rangle - i \int d\Delta f(\Delta) g^* \langle \hat{\sigma}_-(\Delta, t) \rangle. \quad (7)$$

It should be noted that, unlike previous approaches [53, 54], we consider both an inhomogeneous distribution of TLS and a free-space multimode field. Therefore, the right-hand sides of Eqs. (6) and (7) contain the integrals over all field frequencies and detunings, respectively. This leads to the system of coupled integro-differential equations, which in general case can only be solved numerically. Before the rephasing pulse, the inversion parameter is  $s = -1$ . The inhomogeneous distribution is assumed Gaussian,

$$f(\Delta) = \frac{N_{\text{TLS}}}{\sqrt{2\pi} \sigma_{\Delta}} \exp\left(-\frac{\Delta^2}{2\sigma_{\Delta}^2}\right), \quad (8)$$

with  $\sigma_{\Delta} = \frac{\text{FWHM}_{\Delta}}{2\sqrt{2\ln 2}}$  and  $N_{\text{TLS}}$  the number of excited TLS. The optical input is taken to be a multimode coherent state  $|\alpha\rangle$ , defined by

$$\hat{a}(\omega, t_0) |\alpha\rangle = \alpha(\omega) |\alpha\rangle, \quad (9)$$

with a Gaussian coherent spectral amplitude

$$\alpha(\omega) = \alpha_0 \frac{1}{\sqrt{\sigma_{\omega}} \pi^{1/4}} \exp\left(-\frac{\omega^2}{2\sigma_{\omega}^2}\right) \exp(-i\omega t_0), \quad (10)$$

where the phase factor  $\exp(-i\omega t_0)$  sets the temporal offset of the incident pulse such that it impinges on the

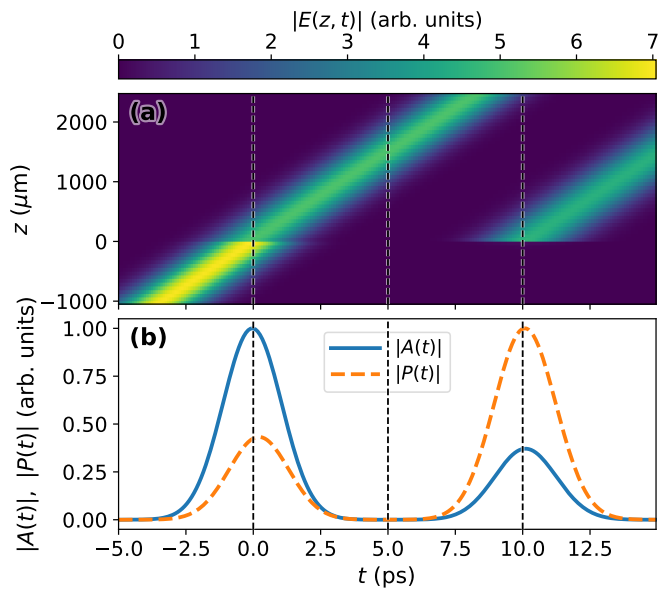


FIG. 8. Electric field amplitude and integrated observables. (a) Reconstructed field  $E(z, t)$  shown as a function of propagation coordinate  $z$  and time  $t$ . (b) Corresponding integrated field amplitude  $|A(t)|$  and polarization  $|P(t)|$ .

sample at  $t = 0$ . The sample is initially unexcited, i.e.,  $\langle \hat{\sigma}_-(\Delta, t_0) \rangle = 0$ .

At time  $t = \tau_{12}$ , an ideal  $\pi$  pulse is applied. Its effect is incorporated through the boundary conditions

$$\langle \hat{a}(\omega, \tau_{12}^+) \rangle = \langle \hat{a}(\omega, \tau_{12}^-) \rangle, \quad (11)$$

$$\langle \hat{\sigma}_-(\Delta, \tau_{12}^+) \rangle = \langle \hat{\sigma}_-(\Delta, \tau_{12}^-) \rangle^*, \quad (12)$$

together with a sign change of the inversion parameter to  $s = 1$  for  $t > \tau_{12}$  due to the  $\pi$  rotation.

The positive-frequency field is reconstructed as

$$E^{(+)}(z, t) = \int d\omega \mathcal{E}(\omega) e^{ik(\omega)z} \langle \hat{a}(\omega, t) \rangle, \quad (13)$$

with a spectral prefactor  $\mathcal{E}(\omega)$ , which in the present calculations is taken in arbitrary units. Equation (13) is an expansion into delocalized plane wave modes ( $\propto \exp(ik(\omega)z)$ ) with the linear dispersion relation  $k(\omega) = \omega/c$ . The total field is obtained as  $E(z, t) = 2\text{Re}[E^{(+)}(z, t)]$ . We introduce mode-integrated quantities

$$A(t) = \int d\omega \langle \hat{a}(\omega, t) \rangle, \quad (14)$$

$$P(t) = \int d\Delta f(\Delta) \langle \hat{\sigma}_-(\Delta, t) \rangle, \quad (15)$$

where  $A(t)$  is the mode-integrated field amplitude and  $P(t)$  is the macroscopic polarization.

Equations (6) and (7) are solved numerically with parameters listed in Table II. Figure 8 shows the electric field  $E(z, t)$  and the integrated observables  $A(t)$  and  $P(t)$ .

TABLE II. Simulation parameters used in Fig. 8.

Quantity	Value
$n_\Delta$ (grid points)	1000
$n_\omega$ (grid points)	1000
$\Delta_{\min}, \Delta_{\max}$	-20 meV, 20 meV
$\omega_{\min}, \omega_{\max}$	-20 meV, 20 meV
FWHM $_\Delta$	5 meV
$N_{\text{TLS}}$	$2 \times 10^6$
$g$	$1.7 \times 10^{-4}$ meV
$t_0$	-5 ps
$\tau_{12}$	5 ps
$\alpha_0$	$\sqrt{15}$
FWHM $_\omega$	1 meV

The electric field propagates from  $z_1 = ct_0 < 0$  towards the sample at  $z = 0$ . During the interaction with the sample, its amplitude is reduced due to absorption, after which the transmitted field continues to propagate. The excitation at  $t = 0$  generates a macroscopic polarization as all TLS are excited in phase. For  $0 < t < \tau_{12}$ , the microscopic polarizations dephase which leads to a rapid decay of the macroscopic polarization. Due to the action of the  $\pi$ -pulse, the microscopic polarizations start to rephase at  $t = \tau_{12}$ . At the rephasing time  $t_{\text{echo}} = 2\tau_{12}$ , all microscopic polarization are in phase, and, therefore, a macroscopic polarization  $P(t)$  is generated. Due to the light-matter coupling,  $P(t)$  leads to the emission of a photon echo at  $z = 0$ , from where the echo field propagates.  $A(t)$  corresponds to the field amplitude at the sample position  $E(z = 0, t)$  and clearly displays both the initial excitation and the delayed echo.

In summary, the present free-space multimode treatment, including propagation of the quantum-optical field and an idealized  $\pi$ -pulse rephasing step, demonstrates that photon echoes arise from coherent excitation.

The present description can be generalized to higher-order expectation values and arbitrary quantum states of light. In that case, the same linear light-matter model can be treated at the operator level and solved in terms of transfer functions [55].

## D. Discussion

The observation of pronounced Rabi oscillations in Sec. III A confirms that coherent excitation and rephasing of the exciton ensemble are working properly. However, the PE signal level obtained in the current experiments appears to be surprisingly low. Taking into account the considerable absorption in the sample ( $\alpha L \approx 1.2$  in Fig. 1) and the optimal rephasing condition for the second pulse with an area  $\pi$ , i.e., when all NCs excited by the first pulse contribute to the two-pulse PE signal, one would expect nearly unit efficiency [26]. In this case,

according to estimates based on the NC density and the spectral width of the laser, the number of resonantly excited NCs corresponds to  $N_X \approx 5 \times 10^6$ , implying that the measured signals are at least five orders of magnitude smaller than expected.

We should take into account several factors that reduce the PE efficiency: (i) a cross-polarized configuration with an ensemble of randomly oriented NCs yields only  $(1/5)^2$  of the total PE intensity, as shown in Ref. 17; (ii) imperfect phase matching reduces the signal by a factor of 0.6 (see Sec. II B); (iii) loss of coherence,  $\exp(-4\tau_{12}/T_2) = 0.2$ , calculated for  $\tau_{12} = 73.4$  ps and  $T_2 = 180$  ps; (iv) optical losses in the detection path correspond to a factor of 0.3; and (v) the quantum efficiency is only 0.05 in these particular NCs, further reducing the PE signal [39]. Taking all these factors into account, we estimate the maximum number of detected photons to be around 300, which is only about one order of magnitude larger than the maximum signal of 30 observed for the  $\pi/2$ - $\pi$  sequence. Such a difference is acceptable, considering that the exact NC density in the sample is not precisely known.

Note that the absorption spectrum in Fig. 1 does not accurately reflect the number of NCs for which excitons can be treated as two-level systems. For instance, the  $\pi/2$  pulse contains approximately  $10^8$  photons while the number of NCs involved in our measurement is about 20 times smaller. In this case, most absorption occurs in a much larger number of NCs that are excited quasi-resonantly via phonon-assisted transitions, as recently discussed in Ref. 17. In our experiment, only the zero-phonon transitions contribute to the coherent signal. This interpretation is further supported by the observation of strong bleaching and negligible stimulated emission in pump-probe measurements, where no Rabi oscillations are detected in the transmission (see Appendix B). These results suggest that only a small fraction of NCs contributes to the PE emission, leading to an overall low efficiency and preventing the detection of other signals, such as amplified spontaneous emission. To overcome this limitation, further optimization of NC growth toward more homogeneous ensembles is required. Additionally, resonant excitation of trion states could help to suppress fine-structure effects.

It is worth mentioning that photon echo formation occurs as a result of interference at very low signal levels, with only a few photons per PE pulse. In this regime, we begin to approach the quantum limit without significant noise from spontaneous emission. This feature is inherent to homodyne detection with picosecond time resolution. It allows for filtering of the signal at the appropriate delay, which is two to three orders of magnitude shorter than the exciton lifetime of approximately 1 ns in the studied NCs [56].

## IV. CONCLUSIONS

We have studied the photon statistics of PE signals at cryogenic temperature in an ensemble of CsPbI<sub>3</sub> perovskite nanocrystals. We demonstrate coherent control of excitons by detecting pronounced Rabi oscillations of the photon echo for pulse areas up to  $2\pi$  under selective resonant excitation of zero-phonon excitons using spectrally narrow picosecond pulses. The damping of the Rabi oscillations is attributed to spatial inhomogeneity of the excitation (transverse beam profile and the finite optical thickness of the sample) as well as to excitation-induced dephasing. The latter is evidenced by the dependence of coherence time on the excitation strength, where  $T_2$  decreases non-monotonically from 210 to 100 ps. The low efficiency, due to the small number of nanocrystals involved in the photon echo sequence, results in a low number of photons per pulse despite the significant absorption in the sample. Numerical simulations demonstrate the formation of photon echoes in a quantized free-space multimode description.

Using an optical homodyne detection scheme, we analyze the photon statistics of the resulting photon echo signal via the second-order correlation function and the characteristic function. Independent of area of either pulse, we consistently measure  $g^{(2)}(0) \approx 1$ , and the characteristic function remains within the classical region. These results confirm the classical nature of the photon echo as a coherent emission from an ensemble of emitters under excitation with classical laser pulses. We also note the importance of homodyne detection for reducing noise from spontaneous emission in detection. Future work will focus on applying the presented technique to study other semiconductor nanostructures, as well as different excitonic complexes with higher quantum efficiency and weaker decoherence in ensembles, e.g., trions in lead-bromide perovskite nanocrystals or self-assembled InGaAs quantum dots.

## ACKNOWLEDGMENTS

We acknowledge financial support from the Deutsche Forschungsgemeinschaft (DFG) through the Collaborative Research Centre TRR 142 (project number 231447078, projects A02, A04 and C10).

### Appendix A: Excitation induced dephasing

Here, we discuss the modification of the photon echo decay for different intensities of the first excitation pulse. The data are summarized in Fig. 9. For large excitation intensities ( $\Theta_1 \gtrsim \pi$ ), we observe the following features. First, the decay of the PE with  $\tau_{\text{ref}} = 2\tau_{12}$  does not follow a single exponential. At shorter delays, the decay is faster (see Fig. 9(a)), indicating that a larger exciton population in the NC leads to shorter coherence

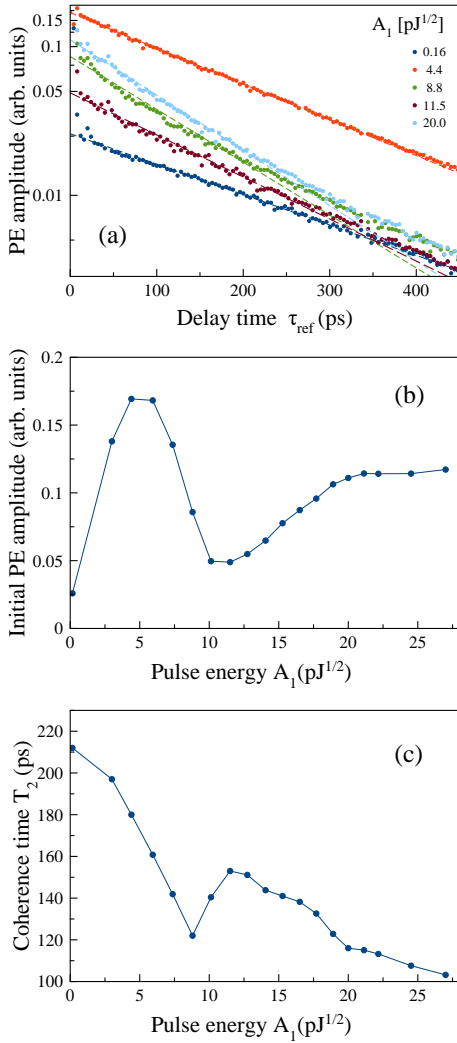


FIG. 9. (a) Set of PE decays for different  $A_1$  and  $A_2 = 9 \text{ pJ}^{1/2}$  ( $\Theta_2 \approx \pi$ ). Dashed lines are fits with exponential decay  $P_0 \exp(-\tau_{\text{ref}}/T_2)$ . (b) Initial amplitude  $P_0$  as function of  $A_1$ . (c) Dependence of the exciton coherence time  $T_2$  on  $A_1$ .

time. Second, the dependence of  $T_2$  is non-monotonic and shows a dip at  $\Theta_1 = \pi$  (compare Figs. 9(b) and 9(c)), corresponding to the largest exciton population in the resonantly addressed NCs. Both features highlight the role of excitation-induced dephasing, which increases with increasing exciton population.

### Appendix B: Bleaching vs amplification

We use a colinear pump-probe scheme to evaluate the bleaching and amplification effects (see inset in Fig 10). The sample is excited by two cross-polarized laser pulses separated by a delay time of 32 ps. The intensity of the second (probe) pulse is strongly attenuated to about 23

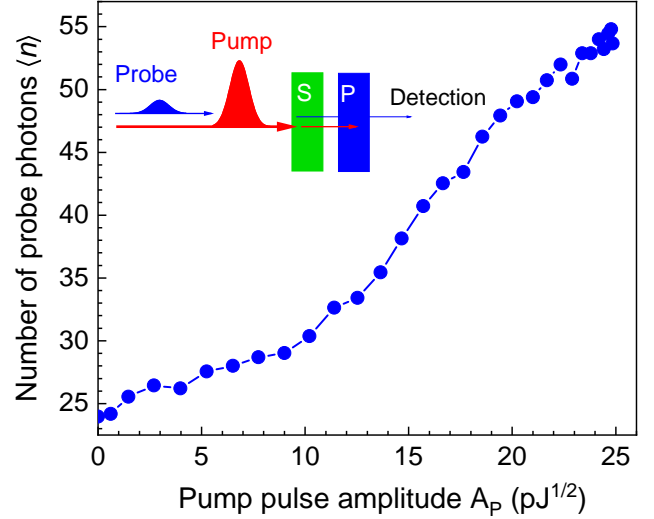


FIG. 10. Transmitted probe intensity as a function of pump pulse amplitude  $A_P$ . Inset shows the scheme of experiment. S - sample, P - polarizer.

photons per pulse. Its transmitted intensity is recorded as a function of the amplitude of the first (pump) pulse  $A_P$ , which is varied from 0 to  $25 \text{ pJ}^{1/2}$  (corresponding to the pulse area  $\Theta_P \approx 0 - 2.8\pi$ ). A polarizer is introduced in the detection path to selectively transmit the probe pulse while strongly suppressing scattered light from the pump pulse.

The dependence of the transmitted intensity of the second pulse in the number of photons is presented in Fig. 10. The signal monotonically increases from 23 to 55 when the pulse area continuously varies from 0 to  $2.8\pi$ . As seen from Fig. 10, we do not observe Rabi oscillation in the transmitted intensity. If, for  $\Theta_P = \pi$ , all nanocrystals with excitons resonant with the pump photon energy were populated, one would expect a peak in transmission at the pump pulse energy  $A_P = 9 \text{ pJ}^{1/2}$  due to stimulated emission initiated by the probe pulse. This peak would then be followed by a decrease for larger pump pulse areas. Instead, the transmission monotonically increases by about a factor of 2, i.e., it does not exceed the overall absorption of 70% which is shown in Fig. 1. This points to the fact that we mainly observe the bleaching of absorption rather than amplification of the second pulse.

Strong bleaching and negligible amplification can be explained as follows. The number of excitons that contribute to non-linear coherent signals such as PE, i.e., can be described as two-level systems, is significantly smaller than the total number of NCs excited by the laser pulses. Most excitons in NCs undergo fast energy relaxation into the lower-energy states within the first 10 ps [17]. The absorption of such NCs is bleached, but they do not contribute to stimulated emission initiated by the second pulse because these excitons are no longer resonant with it. Such NCs also do not contribute to the two-pulse PE

signal for  $\tau_{12} > 10$  ps. As a result, the overall absorption is reduced, but the number of resonant excitons remains too small to produce amplification. This explains the

absence of amplified spontaneous emission and the weak photon echo signals observed in the present study, even though the regime of Rabi flops is well established.

- 
- [1] A. Dey, J. Ye, A. De, E. Debroye, S. K. Ha, E. Bladt, A. S. Kshirsagar, Z. Wang, J. Yin, Y. Wang, L. N. Quan, F. Yan, M. Gao, X. Li, J. Shamsi, T. Debnath, M. Cao, M. A. Scheel, S. Kumar, J. A. Steele, M. Gerhard, L. Chouhan, K. Xu, X. Wu, Y. Li, Y. Zhang, A. Dutta, C. Han, I. Vincon, A. L. Rogach, A. Nag, A. Samanta, B. A. Korgel, C.-J. Shih, D. R. Gamelin, D. H. Son, H. Zeng, H. Zhong, H. Sun, H. V. Demir, I. G. Scheblykin, I. Mora-Seró, J. K. Stolarczyk, J. Z. Zhang, J. Feldmann, J. Hofkens, J. M. Luther, J. Pérez-Prieto, L. Li, L. Manna, M. I. Bodnarchuk, M. V. Kovalenko, M. B. J. Roeflaers, N. Pradhan, O. F. Mohammed, O. M. Bakr, P. Yang, P. Müller-Buschbaum, P. V. Kamat, Q. Bao, Q. Zhang, R. Krahn, R. E. Galian, S. D. Stranks, S. Bals, V. Biju, W. A. Tisdale, Y. Yan, R. L. Z. Hoye, L. Polavarapu, *State of the Art and Prospects for Halide Perovskite Nanocrystals*, ACS Nano **15**, 10775 (2021). <https://doi.org/10.1021/acsnano.0c08903>.
- [2] S. Tsarev, D. Proniakova, X. Liu, E. Wu, G. J. Matt, K. Sakhatskyi, L. L. A. Ferraresi, R. Kothandaraman, F. Fu, I. Shorubalko, S. Yakunin, M. V. Kovalenko, *Vertically stacked monolithic perovskite colour photodetectors*, Nature **642**, 592 (2025). <https://doi.org/10.1038/s41586-025-09062-3>.
- [3] M. L. Zaffalon, A. Fratelli, Z. Li, F. Bruni, I. Cherniukh, F. Carulli, F. Meinardi, M. V. Kovalenko, L. Manna, S. Brovelli, *Ultrafast Superradiant Scintillation from Isolated Weakly Confined Perovskite Nanocrystals*, Adv. Mater. **37**, 202500846 (2025). <https://doi.org/10.1002/adma.202500846>.
- [4] N. E. Kopteva, D. R. Yakovlev, E. Yalcin, I. A. Akimov, M. O. Nestoklon, M. M. Glazov, M. Kotur, D. Kudlacik, E. A. Zhukov, E. Kirstein, O. Hordiichuk, D. N. Dirin, M. V. Kovalenko, M. Bayer, *Highly-Polarized Emission Provided by Giant Optical Orientation of Exciton Spins in Lead Halide Perovskite Crystals*, Adv. Sci. **11**, 202403691 (2024). <https://doi.org/10.1002/advs.202403691>.
- [5] N. E. Kopteva, D. R. Yakovlev, E. Yalcin, I. V. Kalitukha, I. A. Akimov, M. O. Nestoklon, B. Turedi, O. Hordiichuk, D. N. Dirin, M. V. Kovalenko, M. Bayer, *Effect of Crystal Symmetry of Lead Halide Perovskites on the Optical Orientation of Excitons*, Adv. Sci. **12**, 202416782 (2025). <https://doi.org/10.1002/advs.202416782>.
- [6] E. Kirstein, N. E. Kopteva, D. R. Yakovlev, E. A. Zhukov, E. V. Kolobkova, M. S. Kuznetsova, V. V. Belykh, I. A. Yugova, M. M. Glazov, M. Bayer, A. Greilich, *Mode locking of Hole Spin Coherences in CsPb(Cl, Br)<sub>3</sub> Perovskite Nanocrystals*, Nat. Commun. **14**, 699 (2023). <https://doi.org/10.1038/s41467-023-36165-0>.
- [7] P. Tamarat, E. Prin, Y. Berezovska, A. Moskalenko, T. P. T. Nguyen, C. Xia, L. Hou, J.-B. Trebbia, M. Zacharias, L. Pedesseau, C. Katan, M. I. Bodnarchuk, M. V. Kovalenko, J. Even, B. Lounis, *Universal Scaling Laws for Charge-Carrier Interactions with Quantum Confinement in Lead-Halide Perovskites*, Nat. Commun. **14**, 229 (2023). <https://doi.org/10.1038/s41467-023-35842-4>.
- [8] A. Ferrando, J. P. Martínez Pastor, I. Suárez, *Toward Metal Halide Perovskite Nonlinear Photonics*, J. Phys. Chem. Lett. **9**, 5612 (2018). <https://doi.org/10.1021/acs.jpcclett.8b01967>.
- [9] G. Rainó, G. Nedelcu, L. Protesescu, M. I. Bodnarchuk, M. V. Kovalenko, R. F. Mahrt, T. Stöferle, *Single Cesium Lead Halide Perovskite Nanocrystals at Low Temperature: Fast Single-Photon Emission, Reduced Blinking, and Exciton Fine Structure*, ACS Nano **10**, 2485 (2016). <https://doi.org/10.1021/acsnano.5b07328>.
- [10] C. Zhu, M. Marczak, L. Feld, S. C. Boehme, C. Bernasconi, A. Moskalenko, I. Cherniukh, D. Dirin, M. I. Bodnarchuk, M. V. Kovalenko, G. Rainó, *Room-Temperature, Highly Pure Single-Photon Sources from All-Inorganic Lead Halide Perovskite Quantum Dots*, Nano Lett. **22**, 3751 (2022). <https://doi.org/10.1021/acs.nanolett.2c00756>.
- [11] Y. Wang, X. Li, X. Zhao, L. Xiao, H. Zeng, H. Sun, *Nonlinear Absorption and Low-Threshold Multiphoton Pumped Stimulated Emission from All-Inorganic Perovskite Nanocrystals*, Nano Lett. **16**, 448 (2016). <https://doi.org/10.1021/acs.nanolett.5b04110>.
- [12] Y. Xu, Q. Chen, C. Zhang, R. Wang, H. Wu, X. Zhang, G. Xing, W. W. Yu, X. Wang, Y. Zhang, M. Xiao, *Two-Photon-Pumped Perovskite Semiconductor Nanocrystal Lasers*, J. Am. Chem. Soc. **138**, 3761 (2016). <https://doi.org/10.1021/jacs.5b12662>.
- [13] M. A. Becker, L. Scarpelli, G. Nedelcu, G. Rainó, F. Masia, P. Borri, T. Stöferle, M. V. Kovalenko, W. Langbein, R. F. Mahrt, *Long Exciton Dephasing Time and Coherent Phonon Coupling in CsPbBr<sub>2</sub>Cl Perovskite Nanocrystals*, Nano Lett. **18**, 7546 (2018). <https://doi.org/10.1021/acs.nanolett.8b03027>.
- [14] A. Liu, D. B. Almeida, L. G. Bonato, G. Nagamine, L. F. Zagonel, A. F. Nogueira, L. A. Padilha, S. T. Cundiff, *Multidimensional Coherent Spectroscopy Reveals Triplet State Coherences in Cesium Lead-Halide Perovskite Nanocrystals*, Sci. Adv. **7**, eabb3594 (2021). <https://doi.org/10.1126/sciadv.abb3594>.
- [15] A. V. Trifonov, S. Grisard, A. N. Kosarev, I. A. Akimov, D. R. Yakovlev, J. Höcker, V. Dyakonov, M. Bayer, *Photon Echo Polarimetry of Excitons and Biexcitons in a CH<sub>3</sub>NH<sub>3</sub>PbI<sub>3</sub> Perovskite Single Crystal*, ACS Photonics **9**, 621 (2022). <https://doi.org/10.1021/acsp Photonics.1c01603>.
- [16] S. Grisard, A. V. Trifonov, I. A. Solovev, D. R. Yakovlev, O. Hordiichuk, M. V. Kovalenko, M. Bayer, I. A. Akimov, *Long-Lived Exciton Coherence in Mixed-Halide Perovskite Crystals*, Nano Lett. **23**, 7397 (2023). <https://doi.org/10.1021/acs.nanolett.3c01817>.
- [17] A. V. Trifonov, M. O. Nestoklon, M.-A. Hollberg, S. Grisard, D. Kudlacik, E. V. Kolobkova, M. S. Kuznetsova, S. V. Goupalov, J. M. Kaspari, D. E. Reiter, D. R.

- Yakovlev, M. Bayer, I. A. Akimov, *Quantum Beats of Exciton-Polarons in CsPbI<sub>3</sub> Perovskite Nanocrystals*, arXiv:2510.14695 (2025). <https://arxiv.org/abs/2510.14695>.
- [18] S. Mukamel, *Principles of Nonlinear Optical Spectroscopy*, Oxford University Press, 1999.
- [19] S. T. Cundiff, *Optical Two-Dimensional Coherent Spectroscopy*, Optics Express **16**, 4639 (2008). <https://doi.org/10.1364/OE.16.004639>.
- [20] S. V. Poltavtsev, I. A. Yugova, I. A. Akimov, D. R. Yakovlev, M. Bayer, *Photon Echo from Localized Excitons in Semiconductor Nanostructures*, Phys. Solid State **60**, 16354 (2018). <https://doi.org/10.1134/S1063783418080188>
- [21] D. Groll, T. Hahn, P. Machnikowski, T. Kuhn, J. Kasprzak, D. Wigger, *Fundamentals of Heterodyne Wave Mixing Spectroscopy: A Tutorial*, Nano Futures **9**, 042601 (2025). <https://doi.org/10.1088/2399-1984/ae108f>
- [22] A.I. Lvovsky, B.C. Sanders, W. Tittel, *Optical Quantum Memory*, Nat. Photonics **3**, 706 (2009). <https://doi.org/10.1038/nphoton.2009.231>
- [23] W. Tittel, M. Afzelius, T. Chanelière, R.L. Cone, S. Kröll, S.A. Moiseev, M. Sellars. *Photon Echo Quantum Memory in Solid State Systems*, Laser Photonics Rev. **4**, 244 (2010). <https://doi.org/10.1002/lpor.200810056>
- [24] S. A. Moiseev, K. I. Gerasimov, M.M. Minnegaliev, and E. S. Moiseev, *Optical Quantum Memory on Macroscopic Coherence*, Phys Rev Lett. **134**, 070803 (2025). <https://doi.org/10.1103/PhysRevLett.134.070803>
- [25] N. Ohlsson, M. Nilsson, and S. Kröll, *Experimental Investigation of Delayed Self-Interference for Single Photons*, Phys. Rev. A **68**, 063812 (2003). <https://doi.org/10.1103/PhysRevA.68.063812>
- [26] J. Ruggiero, J.-L. Le Gouët, C. Simon, and T. Chanelière, *Why the Two-Pulse Photon Echo is Not a good Quantum Memory Protocol*, Phys. Rev. A **79**, 053851 (2009). <https://doi.org/10.1103/PhysRevA.79.053851>
- [27] Y.-Z. Ma, M. Jin, D.-L. Chen, Z.-Q. Zhou, C.-F. Li, and G.-C. Guo, *Elimination of Noise in Optically Rephased Photon Echoes*, Nature Communication **12**:4378 (2021). <https://doi.org/10.1038/s41467-021-24679-4>
- [28] S. E. Beavan, M. P. Hedges, and M. J. Sellars, *Demonstration of Photon-Echo Rephasing of Spontaneous Emission*, Phys. Rev. Lett. **109**, 093603 (2012). <https://doi.org/10.1103/PhysRevLett.109.093603>
- [29] P. Borri, W. Langbein, S. Schneider, and U. Woggon, R. L. Sellin, D. Ouyang, and D. Bimberg *Ultra-long Dephasing Time in InGaAs Quantum Dots* Phys. Rev. Lett. **87**, 157401 (2001). <https://doi.org/10.1103/PhysRevLett.87.157401>
- [30] W. Langbein and B. Patton, *Microscopic Measurement of Photon Echo Formation in Groups of Individual Excitonic Transitions*, Phys. Rev. Lett. **95**, 017403 (2005). <https://doi.org/10.1103/PhysRevLett.95.017403>
- [31] J. Kasprzak, B. Patton, V. Savona, and W. Langbein, *Coherent Coupling between Distant Excitons Revealed by Two-Dimensional Nonlinear Hyperspectral Imaging*, Nature Photon **5**, 57 (2011). <https://doi.org/10.1038/nphoton.2010.284>
- [32] M. G. Raymer, A. H. Marcus, J. R. Widom, and D. L. P. Vitullo *Entangled Photon-Pair Two-Dimensional Fluorescence Spectroscopy (EPP-2DFS)*, The Journal of Physical Chemistry **117**, 15559 (2013). <https://doi.org/10.1021/jp405829n>
- [33] D. Wigger, J. Schall, M. Deconinck, N. Bart, P. Mrowiński, M. Krzykowski, K. Gawarecki, M. von Helversen, R. Schmidt, L. Bremer, F. Bopp, D. Reuter, A. D. Wieck, S. Rodt, J. Renard, G. Noguees, A. Ludwig, P. Machnikowski, J. J. Finley, S. Reitzenstein, and J. Kasprzak, *Controlled Coherent Coupling in a Quantum Dot Molecule Revealed by Ultrafast Four-Wave Mixing Spectroscopy*, ACS Photonics **10**, 1504 (2023). <https://doi.org/10.1021/acsp Photonics.3c00108>
- [34] E. Evers, N. E. Kopteva, I. A. Yugova, D. R. Yakovlev, D. Reuter, A. D. Wieck, M. Bayer, and A. Greilich, *Suppression of Nuclear Spin Fluctuations in an InGaAs Quantum Dot Ensemble by GHz-Pulsed Optical Excitation*, npj Quantum Information **7**, 60 (2021). <https://doi.org/10.1038/s41534-021-00395-1>
- [35] A. I. Lvovsky, M. G. Raymer, *Continuous-Variable Optical Quantum-State Tomography*, Rev. Mod. Phys. **81**, 299 (2009). <https://link.aps.org/doi/10.1103/RevModPhys.81.299>
- [36] G. Roumpos, S. T. Cundiff, *Multichannel Homodyne Detection for Quantum Optical Tomography*, J. Opt. Soc. Am. B **30**, 1303 (2013). <https://doi.org/10.1364/JOSAB.30.001303>.
- [37] C. Lüders, J. Thewes, M. Assmann, *Real Time  $g^{(2)}$  Monitoring with 100 kHz Sampling Rate*, Opt. Express **26**, 24854 (2018). <https://doi.org/10.1364/OE.26.024854>.
- [38] A. V. Trifonov, F. Godejohann, O. N. Yakovlev, I. A. Akimov, M. Bayer, M. Aßmann, *Continuous Real-Time Optical Homodyne Detection*, Opt. Express **33**, 17418 (2025), <https://doi.org/10.1364/OE.554370>.
- [39] E. V. Kolobkova, M. S. Kuznetsova, N. V. Nikonorov, *Perovskite CsPbX<sub>3</sub> (X=Cl, Br, I) Nanocrystals in fluorophosphate glasses*, J. Non-Cryst. Solids **563**, 120811 (2021). <https://doi.org/10.1016/j.jnoncrysol.2021.120811>.
- [40] M. O. Nestoklon, E. Kirstein, D. R. Yakovlev, E. A. Zhukov, M. M. Glazov, M. A. Semina, E. L. Ivchenko, E. V. Kolobkova, M. S. Kuznetsova, M. Bayer, *Tailoring the Electron and Hole Landé Factors in Lead Halide Perovskite Nanocrystals by Quantum Confinement and Halide Exchange*, Nano Lett. **23**, 8218 (2023). <https://doi.org/10.1021/acs.nanolett.3c02349>.
- [41] R. W. Boyd, *Nonlinear Optics*, Academic Press, 2020.
- [42] S. V. Poltavtsev, Yu. V. Kapitonov, I. A. Yugova, I. A. Akimov, D. R. Yakovlev, G. Karczewski, M. Wiater, T. Wojtowicz, M. Bayer, *Polarimetry of Photon Echo on Charged and Neutral Excitons in Semiconductor Quantum Wells*, Sci. Rep. **9**, 5666 (2019). <https://doi.org/10.1038/s41598-019-42208-8>.
- [43] Y. Han, W. Liang, X. Lin, Y. Li, F. Sun, F. Zhang, P. C. Sercel, and K. Wu, *Lattice Distortion Inducing Exciton Splitting and Coherent Quantum Beating in CsPbI<sub>3</sub> Perovskite Quantum Dots*, Nat. Mater. **21**, 1282 (2022). <https://doi.org/10.1038/s41563-022-01349-4>
- [44] S. V. Poltavtsev, M. Reichelt, I. A. Akimov, G. Karczewski, M. Wiater, T. Wojtowicz, D. R. Yakovlev, T. Meier, M. Bayer, *Damping of Rabi Oscillations in Intensity-Dependent Photon Echoes from Exciton Complexes in a CdTe/(Cd,Mg)Te Single Quantum Well*, Phys. Rev. B **96**, 075306 (2017). <https://doi.org/10.1103/PhysRevB.96.075306>.
- [45] S. V. Poltavtsev, M. Salewski, Yu. V. Kapitonov, I. A.

- Yugova, I. A. Akimov, C. Schneider, M. Kamp, S. Höfling, D. R. Yakovlev, A. V. Kavokin, M. Bayer, *Photon Echo Transients from an Inhomogeneous Ensemble of semiconductor quantum dots*, Phys. Rev. B **93**, 121304 (2016). <https://doi.org/10.1103/PhysRevB.93.121304>.
- [46] A. N. Kosarev, H. Rose, S. V. Poltavtsev, M. Reichelt, C. Schneider, M. Kamp, S. Höfling, M. Bayer, T. Meier, and I. A. Akimov, *Accurate Photon Echo Timing by Optical Freezing of Exciton Dephasing and Rephasing in Quantum Dots* Commun. Phys. **3**, 228 (2020). <https://doi.org/10.1038/s42005-020-00491-2>.
- [47] S. Grisard, A. V. Trifonov, H. Rose, R. Reichardt, M. Reichelt, C. Schneider, M. Kamp, S. Höfling, M. Bayer, T. Meier, and I. A. Akimov *Temporal Sorting of Optical Multiwave-Mixing Processes in Semiconductor Quantum Dots*, ACS Photonics **10**, 3161 (2023). <https://doi.org/10.1021/acsp Photonics.3c00530>
- [48] S. Grisard, H. Rose, A. V. Trifonov, R. Reichardt, D. E. Reiter, M. Reichelt, C. Schneider, M. Kamp, S. Höfling, M. Bayer, T. Meier, I. A. Akimov, *Multiple Rabi Rotations of Trions in InGaAs Quantum Dots Observed by Photon Echo Spectroscopy with Spatially Shaped Laser Pulses*, Phys. Rev. B **106**, 205408 (2022). <https://doi.org/10.1103/PhysRevB.106.205408>.
- [49] T. Kiesel, W. Vogel, B. Hage, J. DiGuglielmo, A. Sambrowski, R. Schnabel, *Experimental Test of Nonclassicality Criteria for Phase-Diffused Squeezed States*, Phys. Rev. A **79**, 022122 (2009). <https://doi.org/10.1103/PhysRevA.79.022122>.
- [50] S. Ryl, J. Sperling, W. Vogel, *Quantifying Nonclassicality by Characteristic Functions*, Phys. Rev. A **95**, 053825 (2017). <https://doi.org/10.1103/PhysRevA.95.053825>.
- [51] W. Vogel, *Nonclassical States: An Observable Criterion*, Phys. Rev. Lett. **84**, 1849 (2000). <https://doi.org/10.1103/PhysRevLett.84.1849>
- [52] Th. Richter and W. Vogel, *Nonclassicality of Quantum States: A Hierarchy of Observable Conditions*, Phys. Rev. Lett. **89**, 283601 (2002). <https://doi.org/10.1103/PhysRevLett.89.283601>
- [53] P. M. Ledingham, W. R. Naylor, J. J. Longdell, S. E. Beavan, and M. J. Sellars, *Nonclassical Photon Streams Using Rephased Amplified Spontaneous Emission* Phys. Rev. A **81**, 012301 (2010). <https://doi.org/10.1103/PhysRevA.81.012301>
- [54] S. A. Moiseev, S. N. Andrianov and F. F. Gubaidullin, *Efficient Multimode Quantum Memory Based on Photon Echo in an Optimal QED Cavity*, Phys. Rev. A, **82**, 022311 (2010). <https://link.aps.org/doi/10.1103/PhysRevA.82.022311>
- [55] D. Scharwald, T. Meier, and P. R. Sharapova, *Phase Sensitivity of Spatially Broadband High-Gain SU(1,1) Interferometers*, Phys. Rev. Research **5**, 043158 (2023). <https://doi.org/10.1103/PhysRevResearch.5.043158>.
- [56] S. R. Meliakov, E. A. Zhukov, V. V. Belykh, K. V. Kavokin, M. O. Nestoklon, E. V. Kulebyakina, M. L. Skorikov, E. V. Kolobkova, M. S. Kuznetsova, M. Bayer, and D. R. Yakovlev, *Hyperfine Interaction of Electrons Confined in CsPbI<sub>3</sub> Nanocrystals with Nuclear Spin Fluctuations*, Phys. Rev. B **113**, 035304 (2026). <https://doi.org/10.1103/s33c-m6hz>.
- [57] Note that the definition of quadratures is to some degree arbitrary and changing their magnitude corresponds to a redefinition of the value of noise of the vacuum state. Therefore the constant factors arising in this equation depend strongly on this choice and the exact measurement scheme used and therefore differ significantly in the literature.